G. Gibertini, J.C. Boniface, A. Zanotti, G. Droandi, F. Auteri, R. Gaveriaux, A. Le Pape
Helicopter Drag Reduction by Vortex Generators
Aerospace Science and Technology, Vol. 47, 2015, p. 324-339
doi:10.1016/j.ast.2015.10.004

Helicopter drag reduction by vortex generators

G. Gibertini[a,*], J.C. Boniface[b], A. Zanotti[a], G. Droandi[a], F. Auteri[a], R. Gaveriaux[b], A. Le Pape[b]

[a] *Politecnico di Milano, Dipartimento di Scienze e Tecnologie Aerospaziali Campus Bovisa, Via La Masa 34, 20156 Milano, Italy*
[b] *ONERA, The French Aerospace Lab, F-92190, Meudon, France*

Abstract

The performance of vortex generators in reducing the helicopter drag was investigated by computational fluid dynamics and wind tunnel tests. Numerical simulations were carried out to define the layout and the position of vortex generators to be tested on a heavy-class helicopter fuselage model. A comprehensive experimental campaign including loads, pressure measurements and stereo particle image velocimetry surveys was then performed to assess the results of the numerical activity. Experiments confirmed the main trends predicted by computations. Tests for an array of vortex generators positioned on the model back-ramp showed a maximum drag reduction of about 5% with respect to the clean geometry. Moreover, the analysis of the velocity field and of the pressure distribution around the backdoor/tail-boom junction enabled to investigate the flow physics related to the effect of vortex generators on the fuselage drag.

Keywords: Helicopters, Wind Tunnel, Vortex generators, Computational fluid dynamics.

*Corresponding author
Email address: giuseppe.gibertini@polimi.it (G. Gibertini)

Nomenclature

Cd	drag coefficient
CFD	Computational Fluid Dynamics
Cp	pressure coefficient
H_{VG}	VG height [m]
L_{VG}	VG chord length [m]
M	Mach number
P	static pressure [Pa]
P_∞	free-stream static pressure [Pa]
PIV	Particle Image Velocimetry
RANS	Reynolds-Averaged Navier-Stokes
Re	Reynolds number
Solidity	Ratio between two VG trailing-edge spacings and VG chord length
U_∞	free-stream velocity [m/s]
VG	Vortex Generator
x_{VG}	Axial position of VG arrays [m]
X	longitudinal coordinate [m]
Y	spanwise coordinate [m]
Z	vertical coordinate [m]
u	longitudinal velocity component [m/s]
v	spanwise velocity component [m/s]
w	vertical velocity component [m/s]
α	angle of attack [deg]
α_{VG}	VG pitch angle [deg]
β	sideslip angle [deg]
δ	Boundary layer thickness [m]
ΔCd	drag coefficient difference evaluated with VG with respect to clean geometry
y^+	Non-dimensional wall distance

1. Introduction

The recent expansion of the helicopter use has drawn the attention on its high environmental impact. Such an impact can be alleviated by decreasing the helicopter fuel consumption and, therefore, by reducing its drag. Among several possibilities, an interesting way to reduce drag is to employ simple passive devices such as vortex generators (VGs).

Vortex generators were widely used to increase the performance at high angles of attack for low speed, delaying the stall by promoting the reattachment of separated flows [13]. In particular, the potential of these devices were also investigated to reduce the aerodynamic drag of blunt ground vehicles operating with high average speed such as trucks or coaches [9, 10]. Potential benefits were also proven for wind turbine applications by lowering noise levels through mitigation of blade stall effects [24] and in rotorcraft applications for the critical issue of alleviating the dynamic stall on the retreating blade side of helicopter rotors [11, 14, 15]. VGs can also improve the efficiency and the range of stable operation of highly loaded compressors, characterising the current trend of the gas-turbine engine design with a notable increase of the thrust-to-weight ratio [7, 17].

Since VGs are inexpensive and can be easily installed also on existing helicopters, they are being considered for drag reduction of blunt helicopter fuselages at cruise speed. Blunt fuselages are characterised by a pronounced upsweep of the after-body shape which is responsible for a recirculating region at the junction with the tail boom, yielding penalties on helicopter drag. Surprisingly, little effort was spent to study the drag reduction effect on a helicopter fuselage equipped with VGs to date. The study of the ef-

fectiveness of these devices was therefore introduced in the work plan of the GRC (Green RotorCraft) project in the framework of Clean Sky programme. The Clean Sky JTI (Joint Technology Initiative) was launched in 2008 as a Public-Private Partnership between the European Commission and the industry. Its mission is to develop technologies that increase the environmental performances of air transport.

Among other platforms, an heavy-weight class helicopter was studied by the GRC2 Consortium. The considered geometry is basically the same one tested in the GOAHEAD project [22] funded by EU's Sixth Framework Programme for Research (FP6). However, in the present investigation the fuselage geometry included the sponsons. Thus, in the following the fuselage geometry is named GOAHEAD-like model. The present paper shows the results of the investigation on the use of VGs for this heavy-weight class helicopter. The study was initially conducted by means of CFD simulations [4]. Then, CFD results were validated by wind tunnel tests, in the ROD (ROtorcraft Drag reduction) GRC2 project.

The vortex generators were installed on the rear door ramp to reduce the corresponding recirculating region. Since the effect of main and tail rotors on the rear ramp wake is expected to be negligible in cruise condition, this study was carried out on a simplified geometry without rotors. The considered geometry is presented in Fig. 1, including the $X - Y - Z$ reference system used in this paper. The $X - Z$ plane is located on the model mid-span plane and the origin of the reference system is positioned on the nose of the fuselage.

Different measurement techniques were employed during wind tunnel

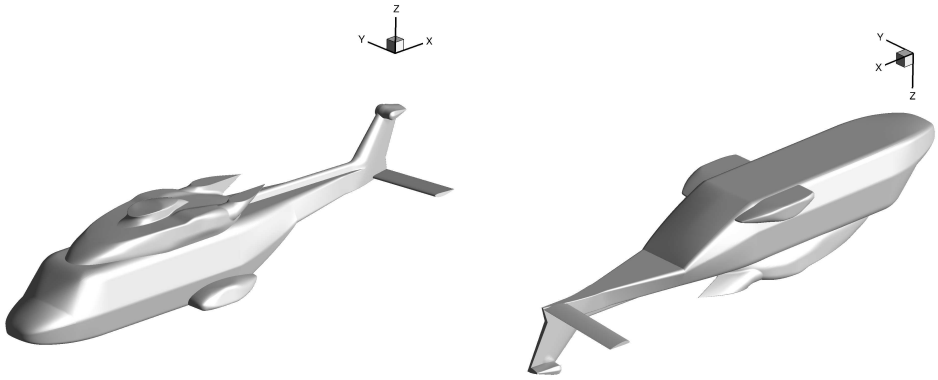

Figure 1: Geometry of the tested GOAHEAD-like model and reference system.

tests. In particular, forces and moments were measured by a six-component strain gauge balance. The mean pressure distribution over the helicopter fuselage was evaluated by steady measurements over 300 taps. Moreover, stereo particle image velocimetry (PIV) surveys were carried out in the region of the junction between the rear ramp and the tail boom to investigate the effects of the best VGs configuration.

The paper is organised as follows. Section 2 describes the computational activity, including the CFD methodology used for the calculations and the results obtained with different sets of VGs characterised by different sizes and positions. Section 3 describes the experimental activity, including the test rig employed for the wind tunnel tests. In section 4 the experimental results are compared with those obtained with the most promising set of VGs indicated by the CFD activity. Section 5 reports the main achievements of the present work.

2. Numerical simulation

2.1. Methodology

All of the CFD computations were performed using the ONERA aerodynamics solver elsA [6]. The RANS equations are discretized in a finite-volume cell-centered formulation on multi-block structured meshes. The simulation of these small control devices scaled according to the local boundary layer thickness required a very high grid density in the nearfield region so that the whole mesh results in a total number of 40×10^6 points. It was found very difficult to perform unsteady computations considering that the time-scale was a-priori unknown for such large separated flow. Furthermore, a very small constant time-step would have required a huge computational time which was not affordable in an assessment study in which numerous VG configurations and angles of attack were investigated. Therefore steady-flow was assumed in all computations. It was numerically experienced that after a long transient phase in which the flowfield remains steady and fully attached, the flow starts separating at the backdoor and the fuselage wake starts oscillating. However, the case of a high Reynolds number flow with relatively fixed flow-separation and flow-reattachement locations is addressed in this paper. Additionally, the most promising tested VG configurations promote flow reattachment and the relative drag reduction obtained can be clearly explained by physical flow mechanisms, even considering a steady assumption. It was also anticipated that the rotating lifting surfaces of the main and tail rotors have little influence on the flowfield underneath the fuselage and will not affect significantly the VG effectiveness, especially at cruise-speed. This is also supported by the work of Allan and Schaffler [1] in which unsteady

effects were investigated for active flow control by zero-net-mass-flux jets, comparing the flow control performance between the isolated fuselage and rotor/fuselage simulations.

A 2nd-order Jameson scheme was used for the space discretisation. The time integration was ensured by a 2nd-order backward Euler scheme and an implicit LU-SSOR phase. The turbulence model used was the $k-\omega$ Kok model with the addition of the Menter's shear stress transport (SST) correction and the Zheng limiter for all computations (Refs. [16],[26]). The simulations presented in this section were considered as being converged once the drag coefficient is stabilised about a mean value.

Regarding the VG representation in the CFD mesh, all CFD computations were carried out by explicitly discretising the vortex generator geometry in the computational mesh within the overset grid method. The motivation for this approach is threefold:

- The vortex generators can be positioned on a discrete surface of the fuselage without requiring to locally adapt or to densify the pre-existing body-fitted fuselage-grid;

- Grid points can be easily clustered around each VG independently of the fuselage grid, drastically reducing the meshing effort;

- Thickness effects of vortex generators can be reproduced computationally unlike external body force models representing the effects of vortex generators based on the lifting-line theory (like the BAY model developed in Ref. [2]).

Basically conventional zero-thickness vane-type VGs with device height

on the order of the local boundary-layer thickness were considered. A dedicated grid generator for VGs was initially developped in the framework of the reduction of secondary flows in high-pressure compressors [5, 20]. This grid generator was designed to discretise a VG configuration within the overset grid method [3]. This approach is especially well suited for parametric studies since a computational mesh can be generated for a single, a pair or even a full array of VGs independently of a pre-existing body-fitted grid. Effects of size, shape, position, number or arrangement of VGs can be then tested numerically without requiring to re-generate a full mesh for a fuselage geometry equipped with VGs. However the grid definition must fulfill a number of constraints in conjunction with the overset grid method, as described in the following.

2.2. Grid definition

The starting point is an existing volume grid for the fuselage geometry and an appropriate post-processing of a reference solution for the clean geometry, allowing to properly place and to characterise the VG dimensions. A detailed schematic of the body-fitted volume grids for the fuselage grid is represented in Fig. 2. The employed fuselage mesh is characterised by a high grid stretching in the normal direction, ensuring an accurate boundary-layer resolution with computed values $y^+ < 1$ in the viscous sub-layer. The VG grids are generated independently on the discrete surface of the fuselage rear-ramp. The VG grid extension in the normal direction is defined such that the VG grids are embedded inside the fuselage grid. The VG grid generator also allows to control the normal distribution of mesh points so that an identical grid refinement to the fuselage grid can be achieved in a large part of

the boundary layer. This is illustrated in the bottom-right of Fig. 2, where the indicated device height approximately corresponds to the local boundary layer thickness. Additionally, the grid extension in the downstream direction and the grid refinement at the VG tip allow the mesh to be fine enough to capture the vortex formation and the convection of vortices downstream with limited effects of numerical dissipation due to grid stretching. Also, a special care must be brought to the longitudial mesh refinement upstream and downstream the VGs, at the boundary overlaps. This is an additional constraint required by the overset grid method in order to achieve a smooth transition with the surrounding fuselage grid. It has been experienced from previous studies that a regular overlap avoids a premature dissipation of the vortices provided that the surrounding volume grid is fine enough downstream of the VG grids. A standard VG grid extension was then adopted with 3 VG chord lengths upstream, 8 VG chord lengths downstream and 3 VG chord lengths normal to the wall. Note that the indicated VG grid extension is not universal. It is problem dependent and it takes into account the mesh quality of the surrounding grid downstream. Tipically, a similar number of grid points is considered for a full array of VGs than for the whole fuselage (see Tab. 1). So the CFD analysis can investigate the performance of small VGs, given the extremely high grid resolution to which the flowfield can be resolved around the VGs. No further grid-refinement study was carried out. As shown later, the grid density as well as the grid extension and the grid overlap downstream the VG array as shown in Fig. 3-right turned out to be sufficient to well capture the vortex core and the vortex path for every single VG.

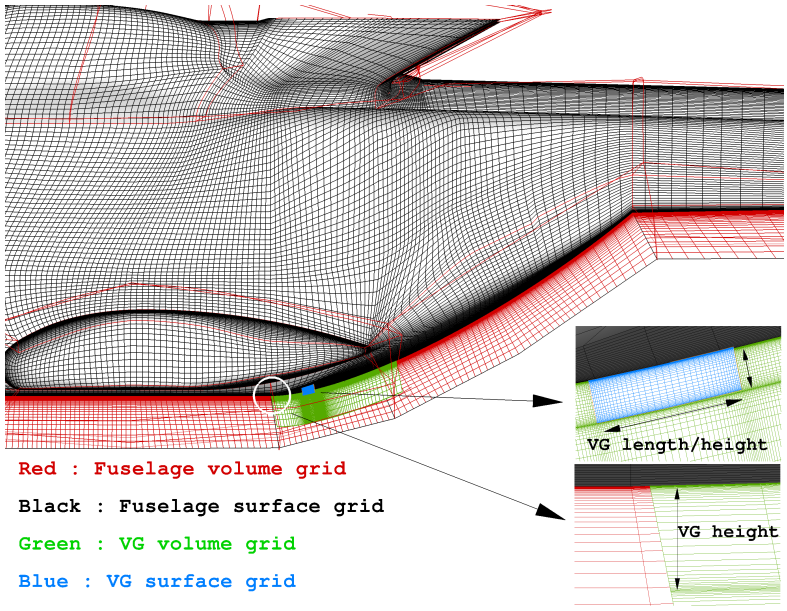

Figure 2: Schematic of the body-fitted grid for the GOAHEAD-like fuselage equipped with VGs

As it can be seen on Fig. 2, the fuselage grid has a limited extension in the normal direction and a farfield grid must be generated accordingly. It is actually important to also carefully define the nearfield grid, especially in the case of the GOAHEAD-like model, for which longitudinal low-pressure vortices in the fuselage near wake may contribute to increase the pressure drag and also drastically reduce the VG effects at some specific angle of attack or sideslip conditions. An intermediate off-body cartesian-grid was then generated in the nearfield from an extended bounding-box in which the whole fuselage grid with VGs is embedded (Fig. 3 left). This cartesian grid was defined with a constant mesh spacing computed from an averaged cell size extracted within the outermost layer of grid cells in the fuselage grid.

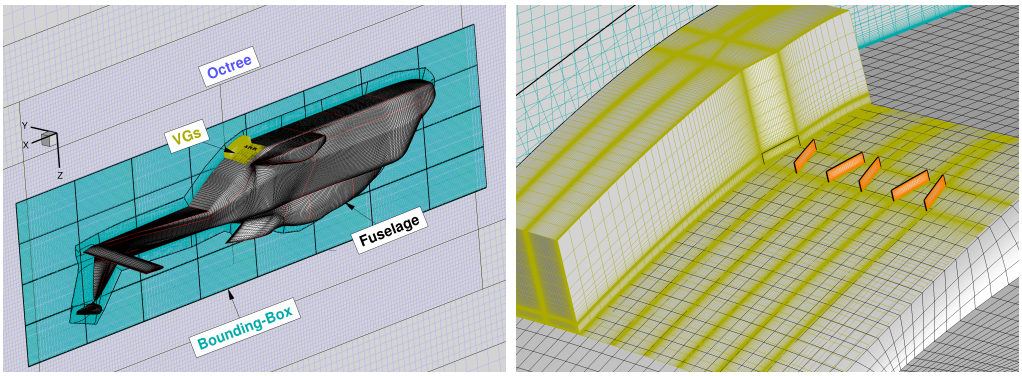

Figure 3: Details of the overset grids for the GOAHEAD-like fuselage equipped with VGs (Left: near and far-field grids, Right: close-up view of the volume grid for a VG array)

Again, this facilitates a smooth transition between overlapping grids and limits the numerical dissipation. The farfield grid is finally generated from the "bounding-box" grid with an adaptive cartesian mesh using the octree approach developed in Ref. [19].

Then, the full structured grid with VGs can be divided into two zones. On one hand, the flowfield in the boundary layer is computed with a high resolution in the curvilinear body-fitted fuselage grid. In the backdoor area where the fuselage grid is blanked out by the overset grid method, the VG mesh is used to compute the vortices trailed away by the array of VGs. On the other hand, the near and farfields are computed in cartesian grids. This yields higher space-accuracy to the flow solver since the finite-volume scheme in curvilinear grids becomes a true second-order accurate finite-difference scheme in cartesian grids with constant spacing. The detail of the mesh density corresponding to the composite mesh used for the CFD computations

is given in Tab. 1.

Table 1: Mesh density for the invidual overlaping grids used for the GOAHEAD-like fuselage with VGs

Mesh	Density (x10^6)
Fuselage	7.75
VGs (single pair)	1
VG array (8 pairs of VGs)	7.6
Bounding-Box	20
Octree	4
Total	40.35

2.3. Results

Additional details of the numerical investigations described in this section can be found in Ref. [4]. Computations were carried out first for the reference solution corresponding to the clean fuselage geometry and then for the controlled configuration with VGs. For a fair comparison between the controlled and uncontrolled cases, computations were performed using exactly the same overset grid system as described previously, except that for the clean geometry, the VG grids are simply removed. The cruise-flight speed corresponds to $U_\infty = 70$ m/s ($M \simeq 0.2$) and the Reynolds number Re is equal to 4.8x10^6 based on the fuselage length (model-scaled configuration). The fuselage attitude was first set to $\alpha = 0°$ during the preliminary CFD investigations. The flow topology at the rear ramp is represented in Fig. 4, with the flow separation at the junction with the tail boom. Performing passive flow control by VGs to alleviate the strong flow recirculation has raised

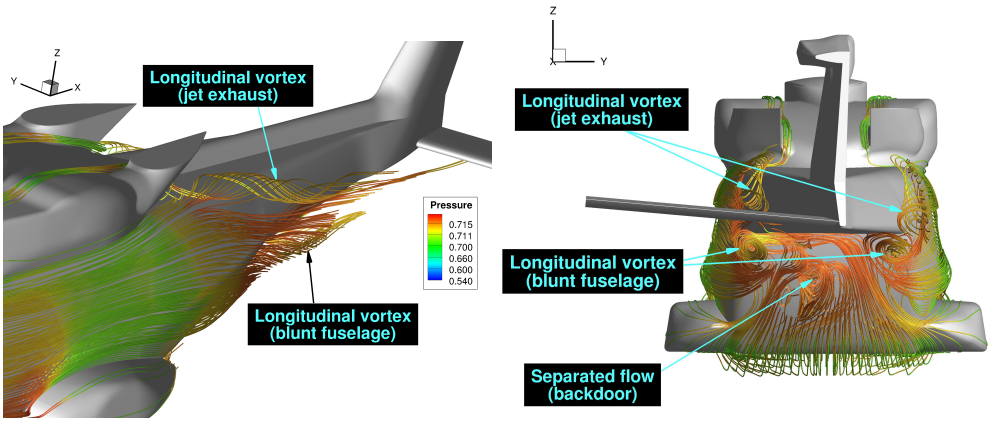

Figure 4: Near wake of the GOAHEAD-like fuselage at cruise speed (streamlines)

a number of concerns regarding the definition of a possible effective VG layouts. As explained in the following, some promising VG layouts were found by considering the blunt fuselage as a ramp problem with three-dimensional effects. Three-dimensional effects are especially characterised by the longitudinal vortices generated from the upper-backdoor due to the strong surface curvature and the jet exhausts as it can be clearly seen in Fig. 4. Additionally, for high nose-down fuselage attitudes, the two sponsons are also responsible for the generation of horseshoe vortices, which may deteriorate the effectiveness of VGs. A simplified ramp model problem described next was precisely designed to assess the effectiveness of VGs, avoiding the critical issues of the three-dimensional geometry.

2.3.1. Ramp model problem

The key-parameters (i.e. first-order parameters) for a preliminary VG design are the position, the size and the pitch angle with respect to the local

velocity field. The model problem was defined by extruding the line defined by the intersection of the symmetry plane with the fuselage surface, including the middle body, the backdoor and tail boom centerlines (see Fig. 5 left). The two-dimensional mesh fits the original normal grid point distribution in the boundary layer. A 3D ramp geometry was built from a spanwise extension of the two-dimensional section, with mirror-like periodicity conditions (see Fig. 5 right). The ramp thus scales exactly with the fuselage geometry and the cruise conditions for $\alpha = 0^\circ$ can be reproduced exactly for the same Reynolds number. The aim of this model problem was to reproduce the strong separated flow, while drastically reducing the CPU time by neglecting 3D effects. The ramp is defined with 21 sections in the spanwise direction, with a total number of grid points of 10^6. To be consistent with the symmetry imposed by the "mirror" boundary condition, only the effectiveness of pairs of counter-rotating VGs in reducing pressure drag could be investigated. Note that for this model problem, the reference solution is purely two-dimensional while the controlled solution is three-dimensional periodic.

A parametric study was conducted in order to first identify the optimal position of the VGs. The VGs were first sized according to an estimate of the boundary layer thickness δ based on the computed displacement thickness with chord length $L_{VG} = 3.6\delta$ and height $H_{VG} = \delta$. The ramp spanwise thickness corresponding to the distance between two symmetry planes was defined with $2.5L_{VG}$. The pitch angle was arbitrarily set to $\alpha_{VG} = \pm 20^\circ$. As expected, a large recirculation occurs for the reference solution (Fig. 6 left). Four VG axial positions $x_{VG} = x_i,\ i = 1, 4$ characterizing the actuation line were considered according to the expected axial position of the separation line

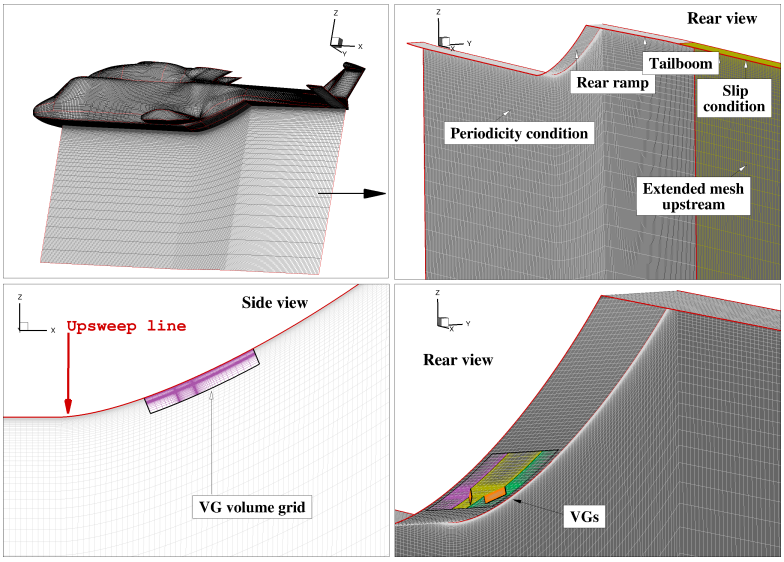

Figure 5: Mesh definition of the ramp model problem used for the primary design of VGs (Top-Left: two-dimensional extruded mesh, Top-Right: three-dimensional mesh with symmetry (mirror-like) conditions, Bottom: details of the overset mesh for the three-dimensional ramp equipped with a pair of counter-rotating VGs)

(Fig. 6 right). It turned out that only the VG pair located at the intermediate position x_2 slightly downstream of the upsweep achieves drag reduction, with $+2.73\%$ found at position x_1, -0.86% at position x_2, $+0,83\%$ at position x_3 and no effect at position x_4, where the flow still separates and no convergence of the flow solver was obtained. It was found a clear correlation between the effectiveness of VGs and a net pressure drag reduction, as illustrated in Fig. 7 for the case of the two axial positions x_2 and x_3 of the counter-rotating VGs. This is a consequence of the local effect of flow regularisation on the static pressure field as it is discussed later in the paper. More unexpected is the

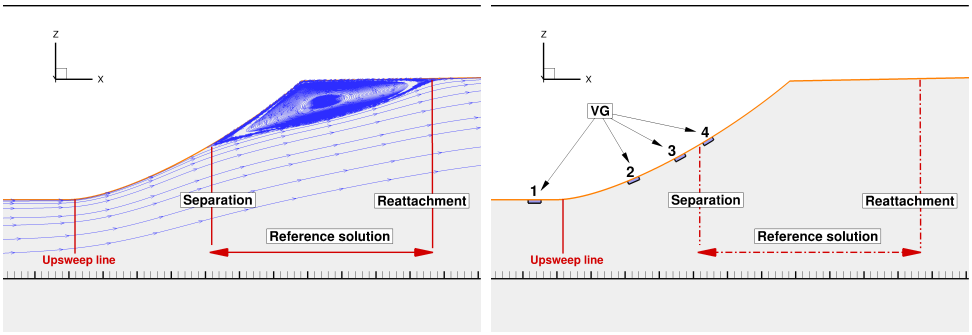

Figure 6: Ramp model problem - Flow recirculation (streamlines) for the reference uncontrolled solution (left) and VG axial positions tested (right)

result at position x_1. By inverting the pitch angle from $\pm 20°$ to $\mp 20°$ with opposite vortices, a drag reduction of -0.7% at position x_1 and -2.64% at position x_2 was found, with a trend similar to the one previously at positions x_3 and x_4. Inverting the pitch angle while applying a symmetry condition actually amounts to shift the symmetry condition in between two counter-rotating VGs. This also modifies the solidity ratio. So it was concluded at that stage that a spurious effect of the arbitary spanwise extension defining the ramp thickness was introduced, with major effects for VG pairs located at the largest distance from the separation line. Nevertheless, it was anticipated that promising drag reduction could be achieved for the GOAHEAD fuselage with VG arrays introduced towards the lower backdoor close to axial position x_2.

Effects of VG dimensions were also tested at axial position x_2, by increasing and decreasing the "reference" device height $H_{VG} = \delta$ by 50% while keeping a constant chord length (see Fig. 8). Together with the pitch angle,

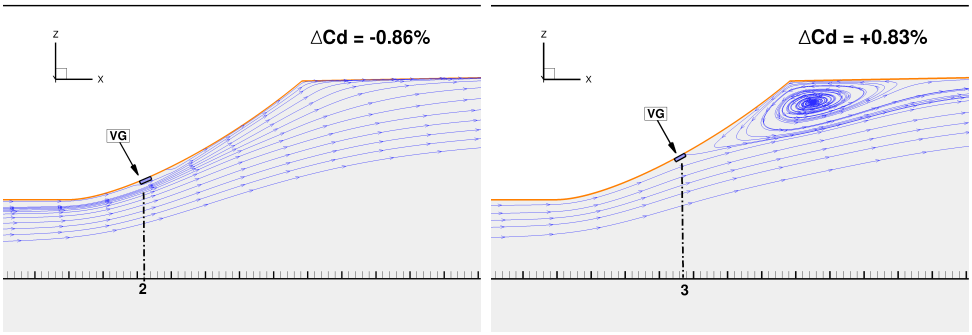

Figure 7: Ramp model problem (streamlines) - Effectiveness of a pair of counter-rotating VGs at axial position x_2 (left) and axial position x_3 (right)

the VG surface has a major impact on the intensity of the pressure variations on both sides of the vortex generator (i.e. the lifting surface with pressure and suction sides) and therefore on the intensity of vortices. For this large separated flow, CFD shows that the effective cancellation of the flow recirculation at the junction backdoor/tailboom is achieved with relatively large (δ-scale) VGs. The larger tested VGs seem more efficient with a drag reduction of -1.42%, although this trend was confirmed neither by the three-dimensional test-matrix nor by experiments. On the other hand, the surprising increase of drag for the smallest VGs is to be related to how the static pressure field is modified at the rear ramp by drastic flow topology changes. So it was concluded that low-profile VGs according to the definition given in Ref. [13] are not appropriate in this case and standard δ-scale VGs were considered for the real fuselage.

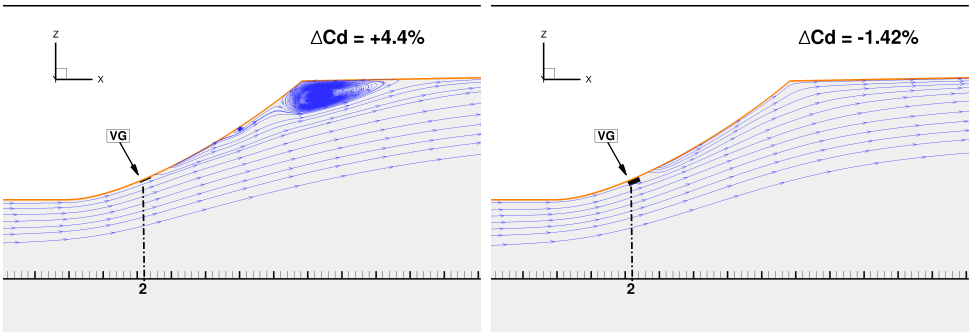

Figure 8: Ramp model problem (streamlines) - Effect of size for the pair of counter-rotating VGs at axial position x_2 (Left: 50% decreased height, Right: 50% increased height)

2.3.2. GOAHEAD-like fuselage

By virtue of the preliminary study carried out for the ramp model problem, a test-matrix investigating configurations for arrays of VGs with unit solidity was defined for the GOAHEAD-like fuselage (see Fig. 9). In order to avoid possible 3D effects, the actuation line was defined at axial position x_2 for all tested arrays of VGs, as identified from the ramp model problem. An example of ill-defined VG layout with increased drag prone to 3D effects can be found in Ref. [4]. The test-matrix was defined to characterise second-order effects basically for the arrangement (i.e. array of symmetrical co-rotating VGs versus counter-rotating VGs). The baseline VG pitch angle was set to $\pm 15^\circ$ in the test matrix. The chord length was left unchanged with respect to the ramp model problem. The effects of a larger pitch angle $\alpha_{VG} = \pm 20^\circ$ and a larger device height ($H_{VG} = 2\delta$) were also investigated. All VG configurations tested experienced a drag reduction between 3.62%

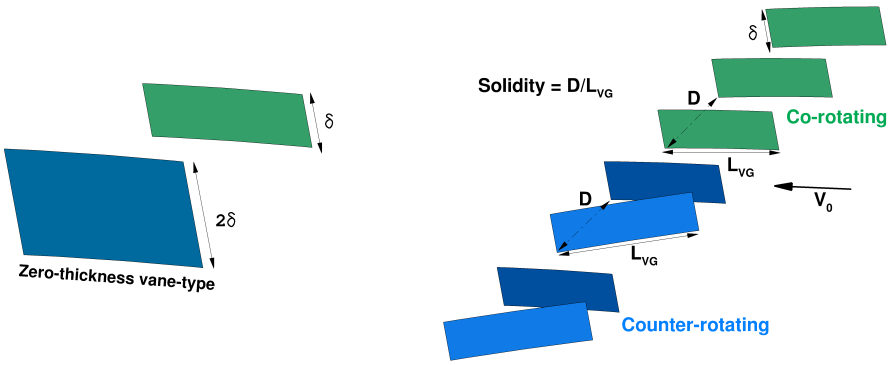

Figure 9: Examples of VGs used in the test-matrix

and 4.91% of the total drag. Results obtained are summarised in the bar chart in Fig. 10. The following trends were obtained (at $\alpha = 0°$):

- A configuration with one array of counter-rotating VGs performs slightly better than 2 symmetric arrays of co-rotating VGs. This is the result of a better mixing between the high momentum entrained by the flow outside of the boundary layer with the low momentum drawn away from surface;

- Any further increase in height as illustrated in Fig. 9-left did not provide a significant drag reduction and did not finally demonstrate its effectiveness also because the device drag is somewhat higher ($\simeq 0.6\%$) than what was found for the smaller δ-scale VGs ($\simeq 0.3 - 0.4\%$);

- For a similar reason but with a major impact, a too high VG pitch angle increases the device drag and reduces the effectiveness of the global VG array. For the co-rotating VGs, a pitch angle increase from $\alpha_{VG} = \pm 15°$ to $\alpha_{VG} = \pm 20°$ experienced a drop of 25% for ΔC_d (see the red and blue bars in the bar chart);

- Arrays of zero-thickness vane-type VGs with pitch angle $\alpha_{VG} = \pm 15^\circ$ and device height $H_{VG} = \delta$ are globally the most effective in drag reduction.

The VG arrays consisting of 2×8 co-rotating and counter-rotating VGs with $\alpha_{VG} = \pm 15^\circ$ as represented in Fig. 12 achieve respectively 4.79% and 4.91% total drag reduction at cruise speed for $\alpha = 0^\circ$. These promising results correspond to a limited device induced drag and a clear flow regularization at the back-ramp characterized by the alleviation of the two large junction vortices occuring for the clean geometry, as illustrated in Fig. 11. All tested VG devices reduce the extent of the separation region but the array of co-rotating VGs with pitch angle $\alpha_{VG} = \pm 15^\circ$ is the most effective in this respect.

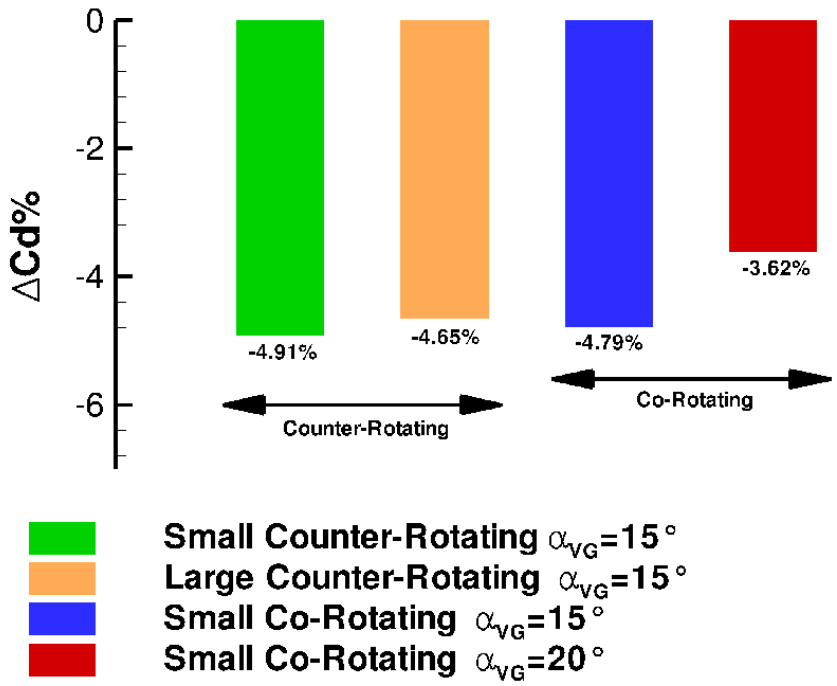

Figure 10: Outcome of the VG test-matrix for the drag reduction ($\alpha = 0°$)

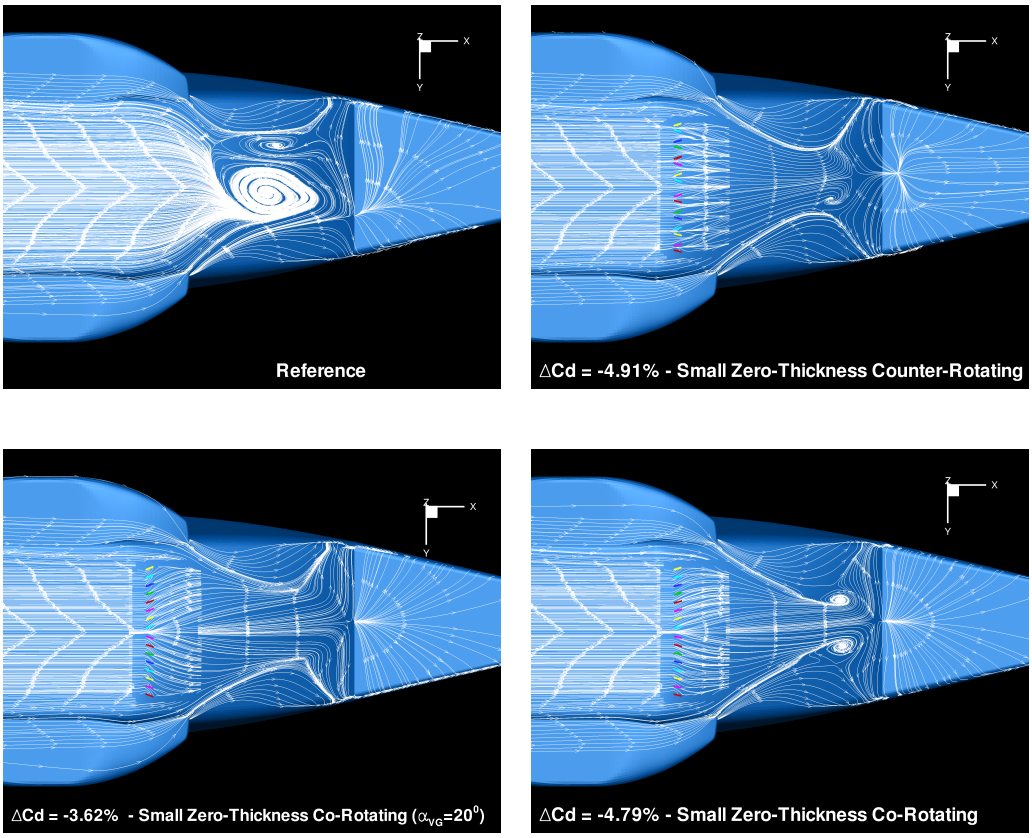

Figure 11: Skin friction patterns for the reference uncontrolled solution (top left), with counter-rotating VGs and pitch angle $\alpha_{VG} = \pm 15°$ (top right), with co-rotating VG and pitch angle $\alpha_{VG} = \pm 20°$ (bottom left) and with co-rotating VG and pitch angle $\alpha_{VG} = \pm 15°$ ($\alpha = 0°$)

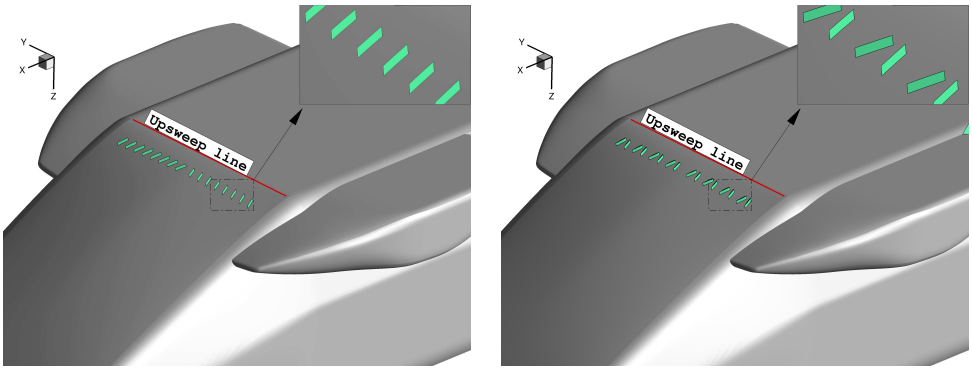

Figure 12: Best arrays of 2 x 8 small (delta-scale) co-rotating VGs (left) and counter-rotating VGs (right) found from the test matrix at axial position $x_{VG} = x_2$

For this fuselage geometry, a fundamental effect of VGs is also to reduce the suction effect at the backdoor, by local static pressure recovery, thus yielding a net decrease of the total drag. This major effect is also reported in Ref. [12] where the drag reduction of a generic helicopter fuselage was investigated by means of active flow control devices. VGs were also tested to reduce the total pressure distorsion and to improve the total pressure revovery within a S-shaped diffusing duct due to flow distorsion at the duct exit (Ref. [18]). This can be clearly seen for an average normalised static pressure in the mid-span symmetry plane plotted on Fig. 13. The flow deceleration at the backdoor responsible for flow separation (with the inflection point in the pressure rise where the flow separates) is reduced with all the tested devices and the adverse pressure gradient is increased with respect to the clean configuration. The turbulent boundary layer is in fact able to sustain the regularly increasing adverse pressure gradient thanks to a more efficient mixing due to the VGs, thus preventing the boundary layer separation. This

effect is more pronounced for the array of counter-rotating VGs.

Additional CFD post-processing was carried out to get a better insight of the vortex cores and vortex trajectories. Thanks to the extremely high grid resolution considered around the VGs, vortex identification by Q criterion represented in Fig. 14 clearly shows the ability of the numerical simulation in representing the details of the device-induced streamwise vortices. Plotting streamlines passing through the vortex cores gives also interesting flow visualisations of the vortex paths (Fig. 15). The top view of the upside-down fuselage shows that the vortex strength and vortex trajectories are not significantly affected by the regular overlap between the fuselage mesh and the VG mesh. These vortical structures are preserved with limited dissipation over large distances also thanks to the cartesian mesh used in the near field with higher accuracy of the flow solver. The side view especially illustrates that the vortices remain close to the boundary layer adjacent to the wall at the lower backdoor up to the highly curved part of the upper backdoor where the uncontrolled flow starts separating.

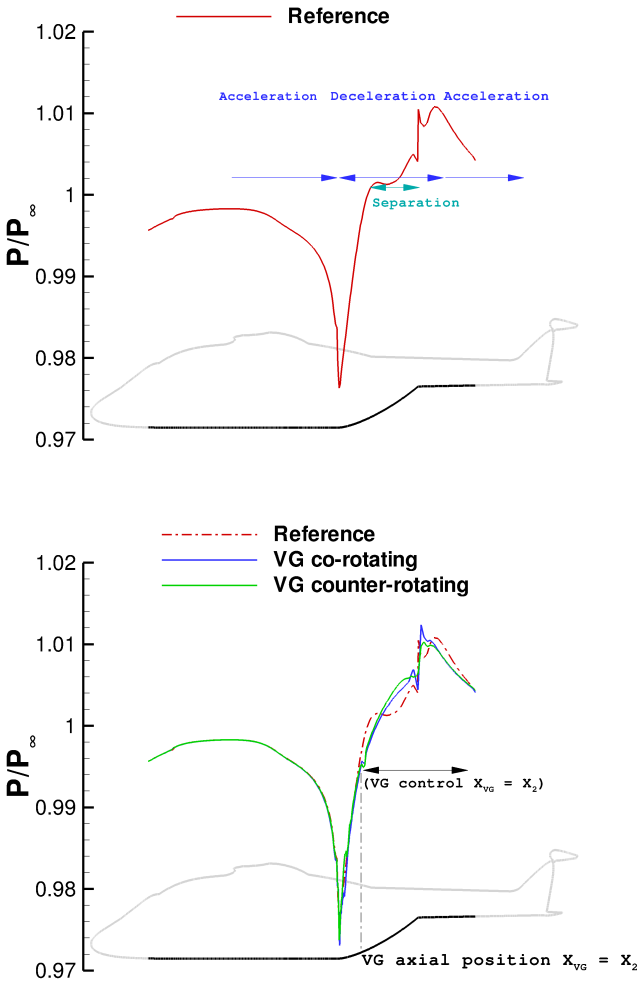

Figure 13: Axial distribution of a spanwise averaged normalised static pressure P/P_∞ in the mid-span symmetry plane for the reference uncontrolled solution (top) and controlled solutions for some relevant tested VG configurations (bottom) at $\alpha = 0°$.

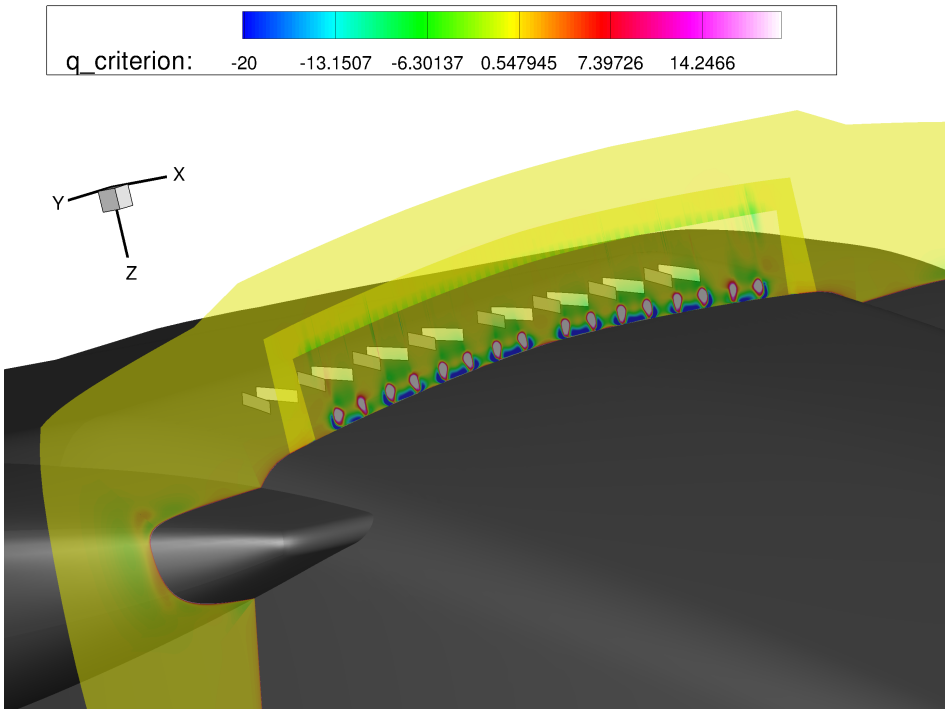

Figure 14: Details of the vortex cores in a CFD-mesh slice downstream of the small counter-rotating VGs with actuation line at axial position $x_{VG} = x_2$ for a normalised Q criterion ($\alpha = 0°$)

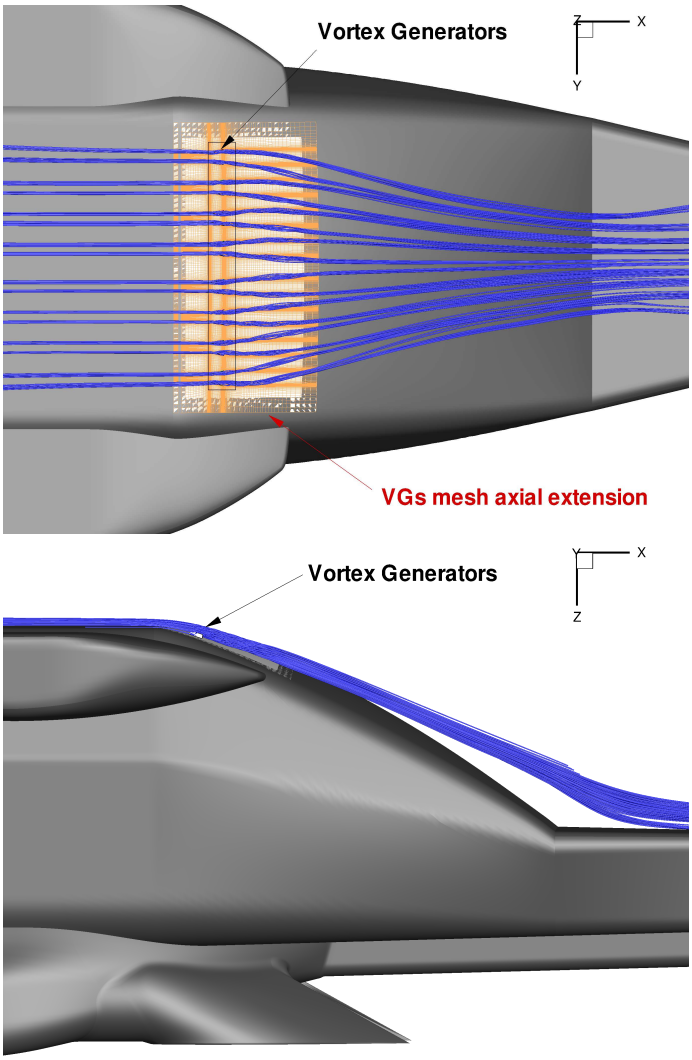

Figure 15: Views of the vortex paths (streamlines) for the counter-rotating VGs at $x_{VG} = x_2$, fuselage upside-down (top) and side view (bottom) ($\alpha = 0°$)

Different fuselage attitudes were also considered for the configuration with small (delta-scale) counter-rotating VGs at axial position x_2 and a sideslip

effect was also tested for the cruise incidence $\alpha = -2°$. Results for the total drag reduction are summarised in Fig. 16. Maximum drag reduction is obtained for angles of attack close to cruise conditions (design point for VGs), and the effects of the VGs are reduced for high negative pitch attitudes (nose-down). This loss of VG efficiency may result from cumulated effects of slight variations of the boundary-layer thickness with the angle of attack and especially from the creation of strong additional horseshoe vortices due to the sponsons as shown in Ref. [4].

The characteristics of the most interesting VGs configurations with angles α, β considered in the CFD assessment are reported in Tab. 2. Experimental results for these 4 VG configurations and the comparison with CFD computations are described in the following.

Table 2: Characteristics of the 4 VG configurations tested in wind tunnel with α, β angles considered by CFD (Large co-rotating VGs not tested by CFD)

VG Configuration	α_{VG}	L_{VG}	H_{VG}	x_{VG}	α	β
Clean geometry	-	-	-	-	$[-12°, +8°]$	$(0°, +5°)$
Small co-rotating	$\pm 15°$	3.6δ	δ	x_2	$0°$	$0°$
Large co-rotating	$\pm 15°$	4δ	2δ	x_2	-	-
Small counter-rotating	$\pm 15°$	3.6δ	δ	x_2	$[-12°, +8°]$	$(0°, +5°)$
Large counter-rotating	$\pm 15°$	4δ	2δ	x_2	$[-2°, +2°]$	$0°$

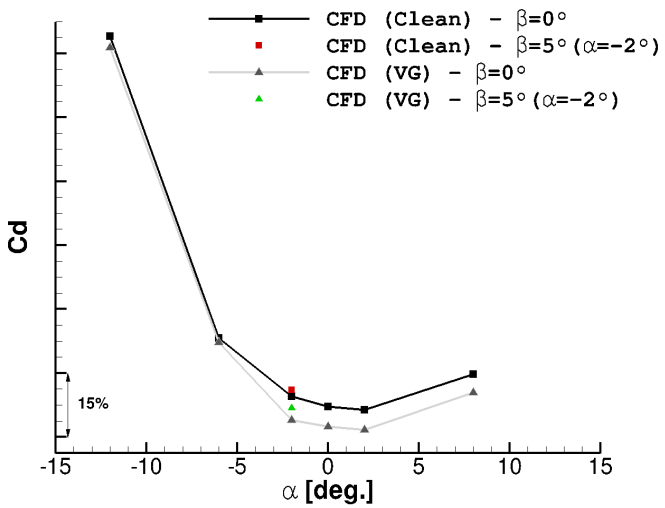

Figure 16: Effect of flow control by small counter-rotating VGs on the drag reduction as a function of α (colour symbols correspond to a sideslip effect at $\alpha = -2$ deg.)

3. Experimental tests

The wind tunnel tests were carried out in the Galleria del Vento of Politecnico di Milano (GVPM), a medium-size facility with a 4 m $\times$ 3.84 m test section. The GVPM is a 1.4 MW closed loop wind tunnel driven by an array of 14 fans. The maximum wind velocity is 55 m/s and the turbulence intensity is less than 0.1%.

The 1/4 scale model for the wind tunnel tests was set up by Politecnico di Milano in the framework of ROD project, starting from some pre-existing components. In particular, the fuselage was the same used for the GOAHEAD project [22](with additional sponsons) and the internal structure had to be re-built to be compatible with the strut of the GVPM facility.

3.1. Test rig

In the framework of ROD project the GOAHEAD-like model was extensively tested in the GVPM facility. The model was fixed to the head of the test-section strut that allows to set both the sideslip and the incidence angles. The strut is fixed to a turning-table on the test-section floor allowing to set the sideslip angle, while its head is articulated to allow one to set the angle of attack of the model. The internal structure of the model was purposely re-designed and built in the frame of ROD project in order to interface the model with the GVPM strut in both upright and upside-down configurations. The upside-down tests were especially addressed to evaluate the performance of the VGs. In fact, when the model is mounted upside-down, the strut is fixed to the helicopter upper side (see Fig. 17). Thus the lower surface (where the vortex generators are located) is not disturbed. All tests were carried out at a wind tunnel free-stream velocity of 50 m/s.

Following CFD indications, four configurations of VGs considered the most interesting were tested in the wind tunnel (see Tab. 2). The VGs were cut from a 1 mm thick PVC sheet and glued on a thin strip made of the same material (0.5 mm thickness and 30 mm chord). A close-up of the small (i.e. δ-scale) counter-rotating array of VGs mounted on the model is shown in Fig. 18.

A six-component RUAG 192-6L strain-gauge internal balance installed inside the model was used to measure the aerodynamic loads and moments. An accuracy of 0.5% of the fuselage drag measured for the helicopter clean geometry can be estimated from the experience acquired on the employed balance, taking also into account that the test procedure was designed to

Figure 17: GOAHEAD-like model mounted in the GVPM wind tunnel.

Figure 18: Close-up view of the VGs mounted on the model (small δ-scale counter-rotating array).

minimise the thermal drift. All the presented data are corrected considering wind tunnel effects.

3.2. PIV set up

Stereo PIV surveys were carried out in the region at the junction between the rear ramp and the tail boom. The system was set up to measure the three velocity components on longitudinal X-Z plane windows at different Y locations. The spacing between the measurement planes in the Y direction was 5 mm over a range of 260 mm centered on the model mid-span section (total number of 53 measurement planes). The area of investigation was 365 mm $\times$ 185 mm and the position of the measurement window is illustrated in Fig. 19. This technique enables to reconstruct the mean three-dimensional flow structures over a volume [25].

The PIV system comprised a Litron NANO-L-200-15 Nd:Yag double pulsed laser with a 200 mJ output energy and a wavelength of 532 nm, and two Imperx ICL-B1921M CCD cameras with a 12 bit, 1952×1112 pixel array. The layout of the PIV instrumentation is illustrated in Fig. 20. The laser was attached to a single-axis traversing system positioned on the top of the wind tunnel test section. The cameras were mounted on two linear guides attached on the side wall of the test section to move the image planes in the Y direction. Each camera was equipped with a Nikkor 50 mm lens and tilting lens mountings for correct focusing of the measurement window. The tilting lens mountings were adjusted in order to achieve the Scheimpflug condition. The camera separation angle was set to 40° to have a proper optical access to the selected measurement area. During the tests, the laser and the cameras were moved simultaneously in the Y direction so that a

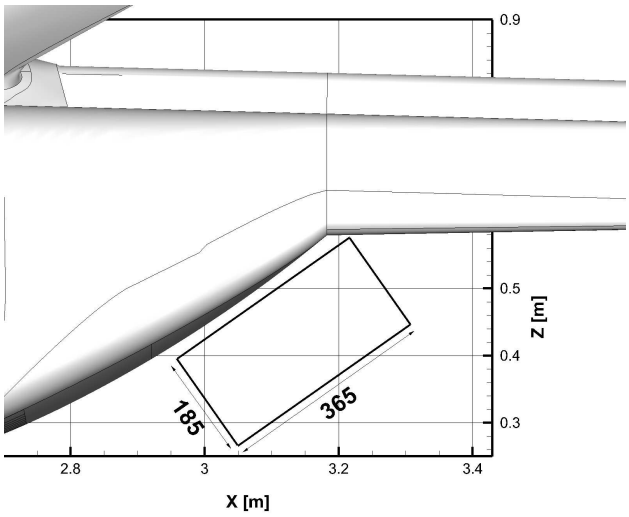

Figure 19: PIV measurement window on the longitunal plane: the dimensions of the window are in mm.

correct focusing of the laser sheet with the image plane was obtained for each measurement window. The synchronisation of the two laser pulses with the image-pair exposure was controlled by a 6-channel Quantum Composer QC9618 pulse generator. A particle generator with Laskin atomizer nozzles was used for the seeding of the entire test-section. The particles consisted of small oil droplets with a diameter in the range of 1-2 μm.

The image-pair analysis was carried out by the PIVview 3C software [21], developed by PIVTEC. In particular, the multigrid interrogation method [23] was used starting from a 96 pixels $\times$ 96 pixel to a 32 pixel $\times$ 32 pixel interrogation window. For more details about the stereo PIV analysis methodology, the reader is referred to the software manual [21]. All the resulting velocity fields presented in this paper were averaged over 100 image pairs. This

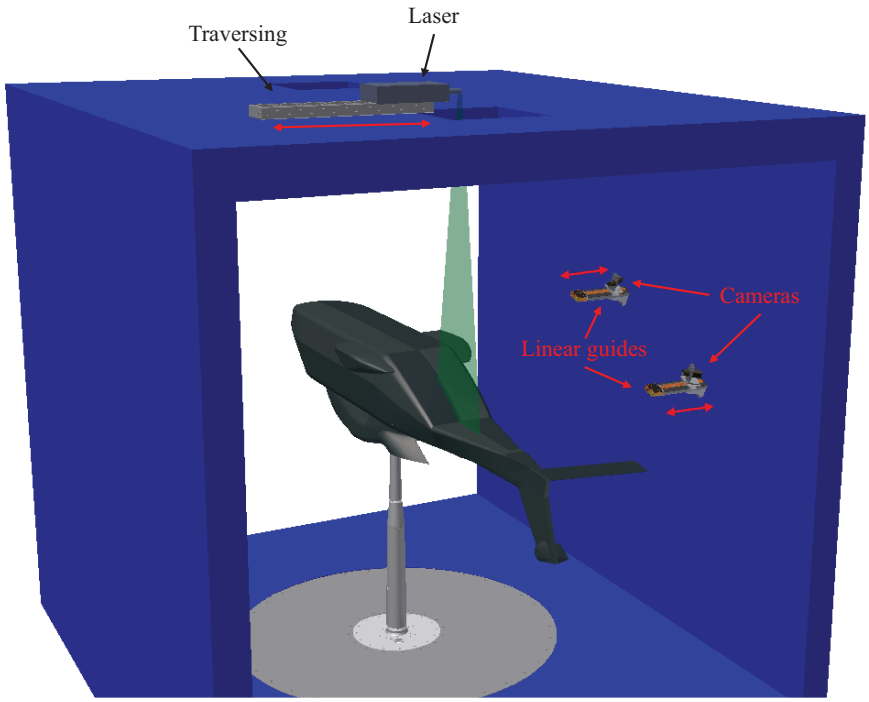

Figure 20: Layout of the PIV instrumentation in the wind tunnel test section.

choice was considered a fair compromise between the need to obtain reliable averages and an admissible run time due to the high number of spanwise measurement windows considered for each run to complete the survey of the volume of interest.

The accuracy of the PIV measurement can be estimated considering a maximum displacement error of 0.1 px, as it was found in Ref. [25]. Taking into account the pulse-separation time and the optical magnification, the maximum in-plane velocity error results to be about 1% of the maximum in-plane velocity component [8]. Due to the stereoscopic optical set-up, a slightly higher error can be estimated for the out-of-plane velocity component.

3.3. Pressure measurements

A series of 300 static pressure taps are distributed on the model surface as illustrated in Fig. 21. Only the sponsons and the exhaust jets are not equipped with pressure taps. The static pressure measurements were carried out by means of 8 pressure scanners (1 PSI F.S., accuracy 0.1% F.S.) installed inside the model. The average pressure distribution was obtained over an acquisition time of 10 s for each angle of attack tested.

4. Comparison between experimental and numerical results

4.1. Drag reduction

In order to evaluate the VGs layout providing the best performance in terms of drag reduction, the four selected arrays of VGs were tested with the model at $\alpha = -1.8°$, representing the cruise angle of attack of the actual

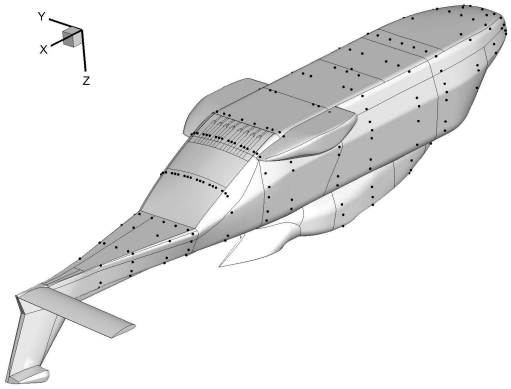

Figure 21: Layout of the pressure taps distribution on the model surface.

helicopter. The tests were performed with the VGs arrays attached on the model surface in the x_2 position, as indicated by the CFD activity. The results of these tests are presented in Fig. 22, showing the differences of the measured drag coefficients with respect to the clean model geometry.

The comparison of the measured drag coefficients shows that the small counter-rotating VGs array produces the highest drag reduction at cruise angle of attack (about 3%), confirming the results of the CFD simulations carried out at $\alpha = 0°$. In particular, the results for the large co-rotating VGs, not tested by CFD, shows that they are not efficient for drag reduction.

Thus, the small counter rotating VGs were therefore selected to be subject of a detailed investigation in the experimental study. Fig. 23 left shows the drag coefficients differences measured with the small counter-rotating VGs array during a sweep of angle of attack.

The tests results show an appreciable reduction of drag due to VGs in the range $-4° \leq \alpha \leq 10°$, with highest drag reduction obtained for $\alpha = 2°$

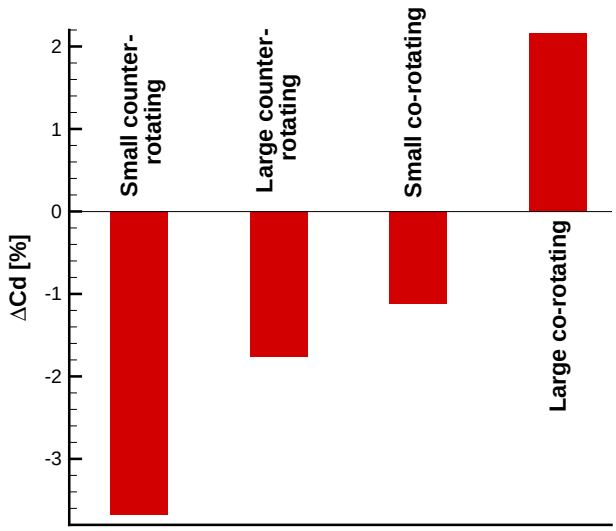

Figure 22: Effect on measured drag of the different arrays of VGs at $\alpha = -1.8°$.

(about 5%). The comparison of CFD and experimental results for the clean geometry presented in Fig. 23 right shows a very good agreement of the drag coefficient difference evaluated with the small counter-rotating VGs, with only exception of the lowest angle of attack considered for the CFD simulation.

4.2. Velocity field

A detailed investigation of the flow physics was carried out for the angle of attack $\alpha = 2°$, where both CFD and experiments show the highest benefit introduced by the small counter-rotating VGs in terms of drag reduction. In the following figures, the comparison of the flowfield around the ramp

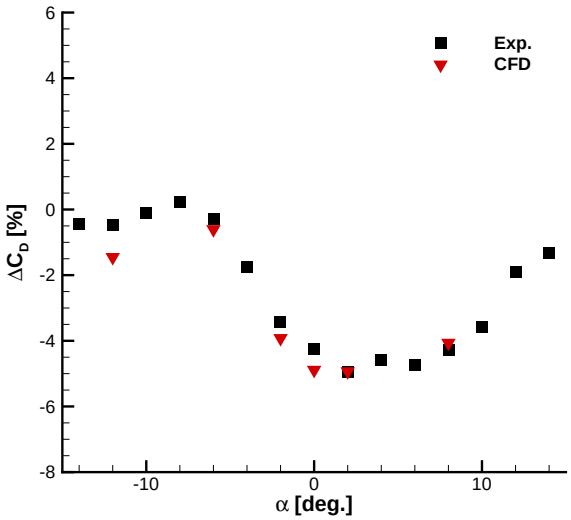

Figure 23: Comparison of the drag difference for the small (δ-scale) counter-rotating VGs.

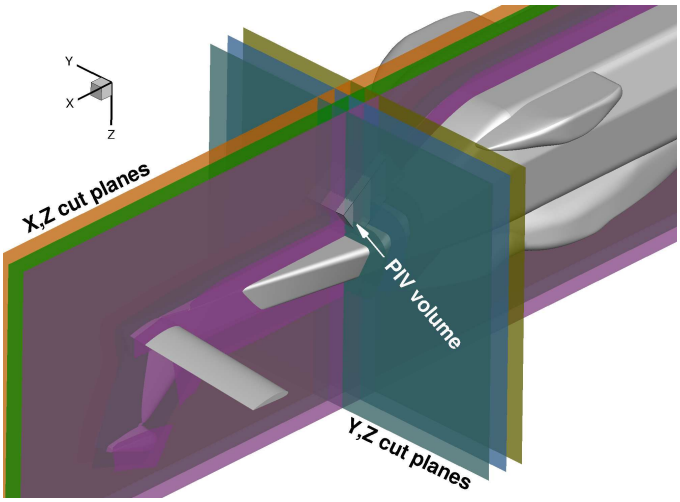

Figure 24: Examples of slices used at the backdoor for CFD/PIV comparison

region evaluated by PIV surveys and CFD is shown for the contours of the non-dimensional velocity components normalised with the free-stream velocity. The averaged PIV data are especially compared with the velocity field extracted at the last computed iteration in different slices as illustrated in Fig. 24. The difference of the free-stream velocity between PIV tests and CFD simulations is not so remarkable to expect important Reynolds or Mach number effects.

Fig. 25 shows the comparison of the non-dimensional longitudinal velocity component u/U_∞ extracted on X-Z planes at different spanwise positions. For the clean geometry configuration, the flow close to the ramp is characterised by a large separation as indicated by the negative values of u evaluated by both CFD and PIV. CFD results show that this separated region is characterised by a large recirculation as can be observed from the in-plane streamlines at Y = 0 m and Y = -0.085 m. The extention of the

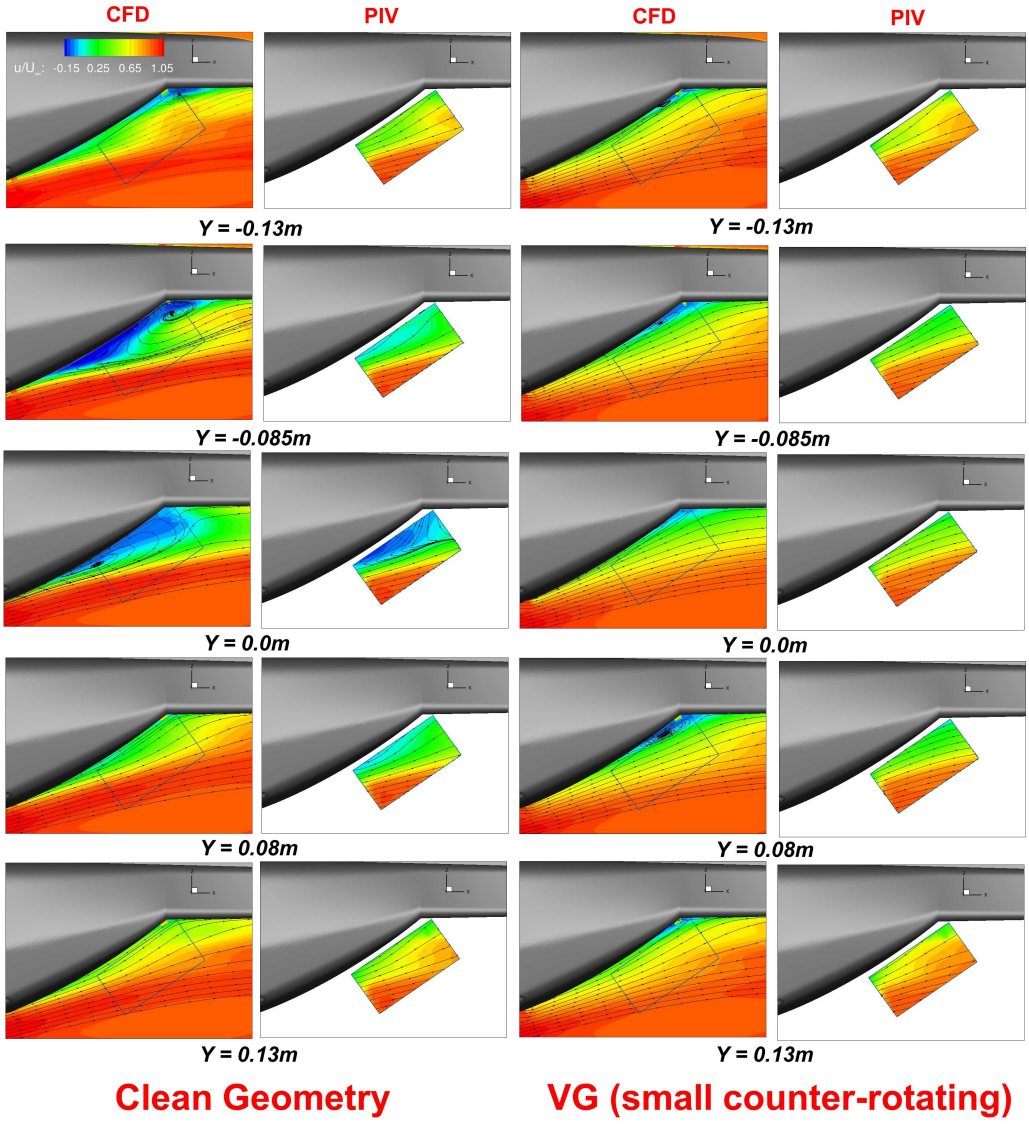

Figure 25: Comparison PIV/CFD at $\alpha = 2°$ for the normalised longitudinal velocity component u/U_∞ on X-Z planes.

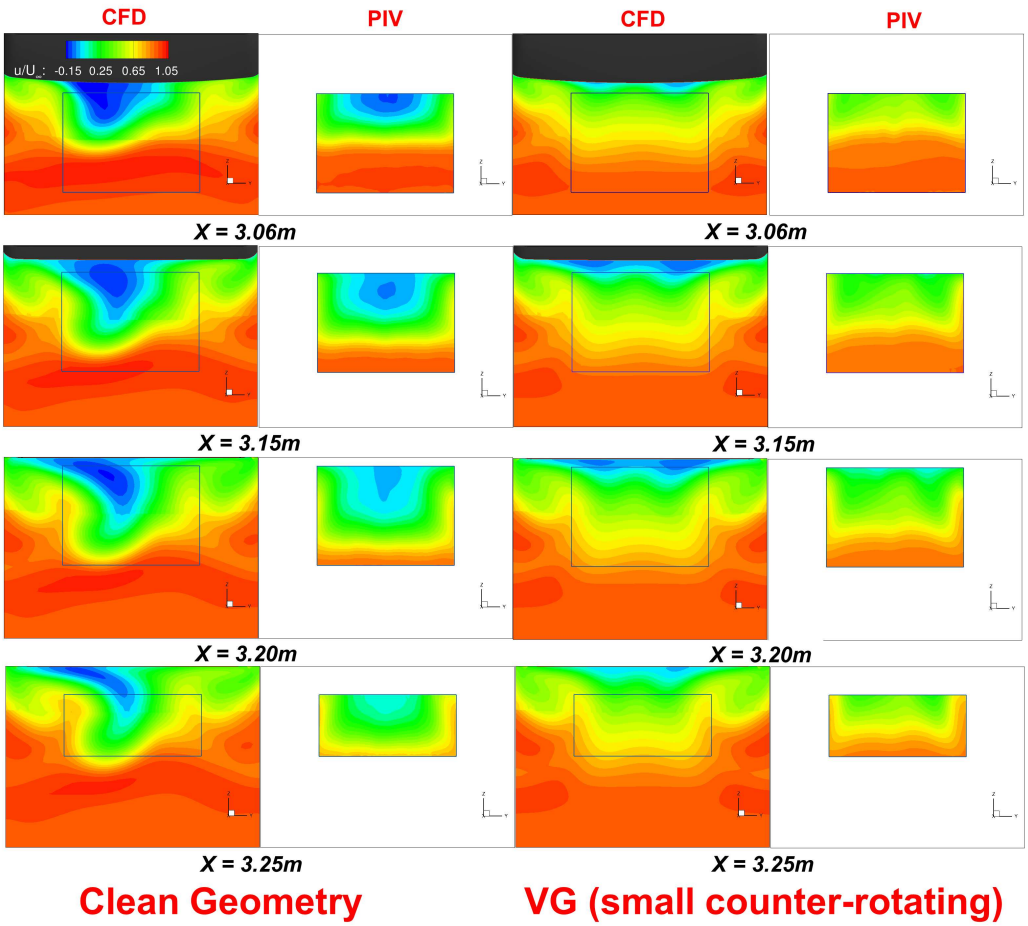

Figure 26: Comparison PIV/CFD at $\alpha = 2°$ for the normalised longitudinal velocity component u/U_∞ on Y-Z planes.

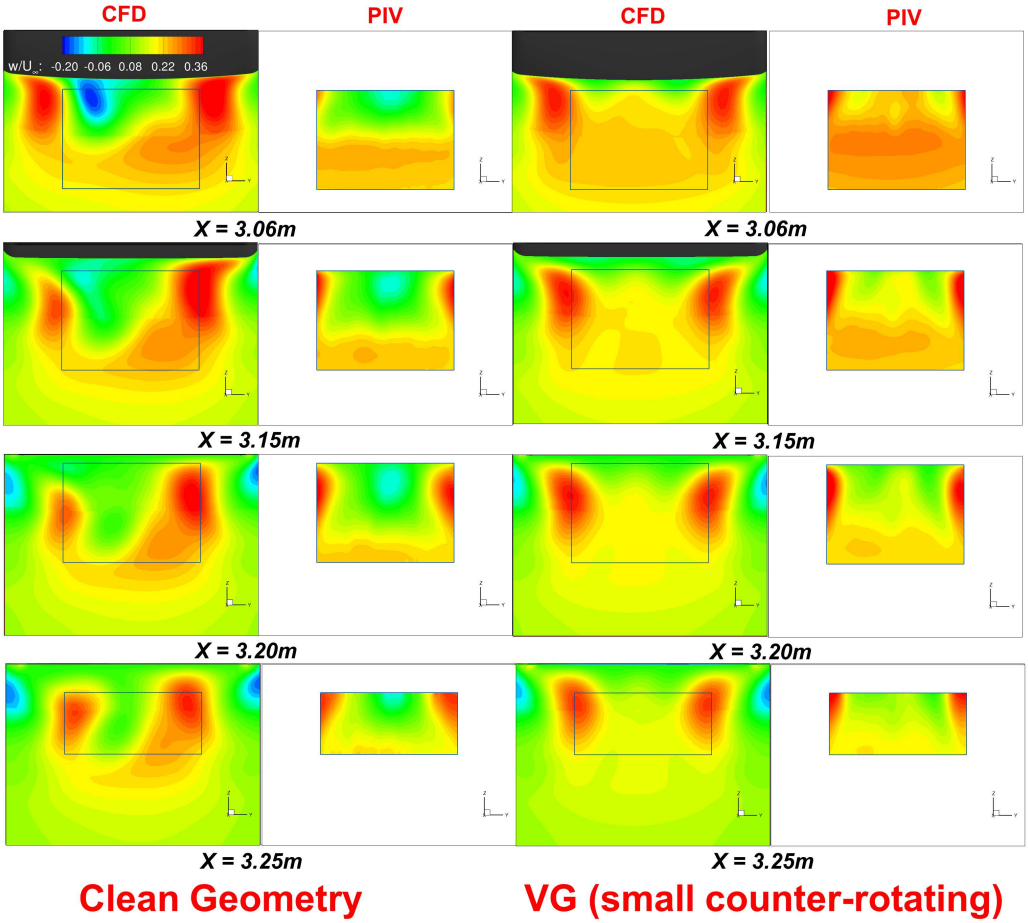

Figure 27: Comparison PIV/CFD at $\alpha = 2°$ for the normalised vertical velocity component w/U_∞ on Y-Z planes.

separated region in clearly appreciable in Fig. 26 showing the comparison of the non-dimensional longitudinal velocity component u/U_∞ extracted in Y-Z planes at different longitudinal positions. A quite good agreement between CFD and PIV results can be observed also on the Y-Z planes, even if time-averaged PIV results show a more symmetrical structure of the separated region with respect to CFD. The non-symmetrical topology of the separated flow evaluated by CFD is highlighted in Fig. 27 showing the contours of the normalised vertical velocity component w/U_∞ extracted on Y-Z planes at different longitudinal positions. The flow topology at the rear-ramp being very sensitive to pressure fluctuations, it is numerically experienced for this geometry that after a transient phase the flow symmetry at the rear-ramp is lost once the flow starts separating. Indeed, a rather high level of velocity fluctuations was found in the measurements for the clean geometry case. On the other hand, the instantaneous 3D flow structure cannot be reconstructed by the PIV planes as they were not simultaneously acquired. In any case, it is reasonable to expect a certain degree of disagreement between a steady simulation and averaged measurements in presence of massive separation and high flow unsteadiness involving the large-scales. In fact, if the instantaneous flowfields obtained by PIV for $X-Z$ plane at Y = -0.085 m are examinated, a large recirculation region similar to the flow obtained by CFD was observed on about 20% of them (see Fig. 28 left). On the other hand, a similar flow pattern was observed for some instantaneous flowfields on the symmetrical plane at $Y = 0.085$ m (again in the order of 20% of them, see Fig. 28 right). This leads to the hypothesis that the solution to which the steady simulation converged essentially corresponds to a possible flow condition of the real un-

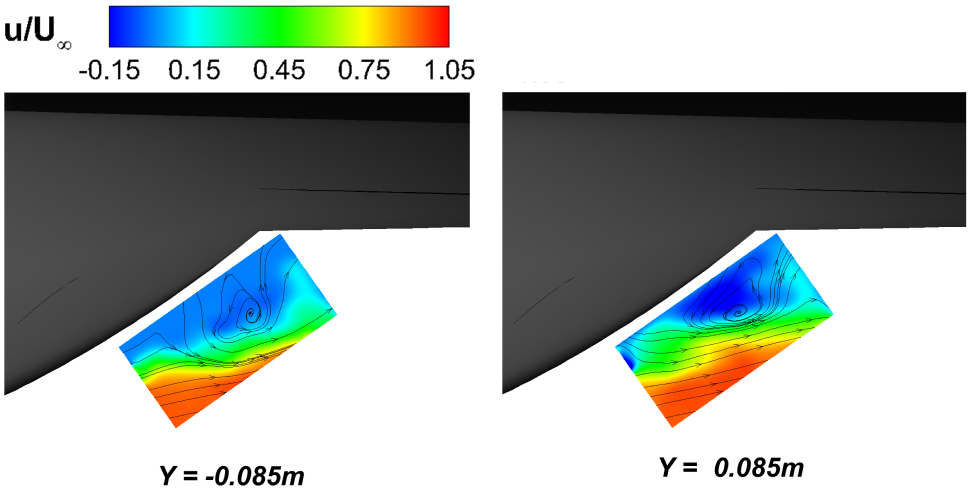

Figure 28: Instantaneous PIV velocity fields at $\alpha = 2°$ for the normalised longitudinal velocity component u/U_∞ on symmetrical X-Z planes.

steady flow where also the symmetrically reflected solution is present for a certain time. In order to find a confirmation of this hypothesis the average of the flowfield obtained by CFD at Y = -0.085 m and the same field reflected with respect to the X-Z plane at $Y = 0$ m was computed and compared with the mean flow obtained by PIV measurements. In fact, as can be observed in Fig. 29, the symmetrised CFD solution shows a good agreement with the phase-averaged velocity field obtained by PIV on the X-Z plane at Y = -0.085.

For the model geometry equipped with the VGs, PIV surveys do not show back-flow region in the volume of investigation, while CFD results show that the flow is still slightly separated close to the backdoor/tail boom junction, as can be observed from the contours of the longitudinal velocity component in the Y-Z planes. Moreover, both PIV and CFD show that this VGs config-

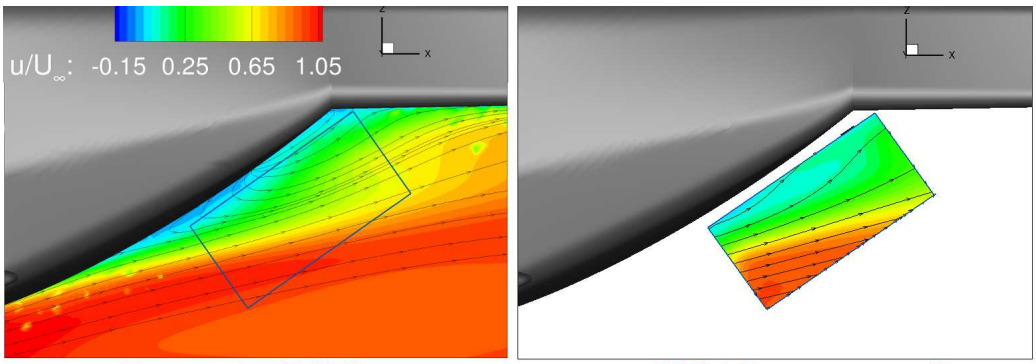

Figure 29: Comparison of the symmetrised CFD velocity field with the phase-averaged PIV measurements at $\alpha = 2°$ for the normalised longitudinal velocity component u/U_∞ on the X-Z plane at Y = -0.085 m.

uration was not designed to control the longitudinal vortical structures issued by the blunt fuselage, as can be observed from the comparison for contours of the vertical velocity component.

4.3. Static pressure

As mentioned earlier, a fundamental effect of the VGs array, when located downstream the pronounced upsweep characterising the blunt fuselage, is twofold. First in re-energising the boundary layer and thus preventing or limiting flow separation and second in triggering a smooth increase of the adverse pressure gradient at the backdoor. PIV constraints cannot allow investigations of the detailed structure of the boundary layer for such a complex geometry. However, pressure measurements confirm the potential benefit of VGs in reducing drag by pressure recovery (i.e. increasing locally the static pressure field) and therefore limiting the suction effect responsible

for pressure drag. This effect is clearly shown in the following from the pressure coefficient distribution. Four instrumented sections were selected at the fuselage surface for a comparison between experimental data and numerical results for the angle of attack $\alpha = 2°$. Sections 1,2 and 3,4 are respectively located outside and inside the effective range of the VGs array respectively. The corresponding comparisons for the Cp coefficient are given in Fig. 30 together with an illustration of the selected sections.

Note that section 2 intersects both sponsons and jet exhausts not instrumented with pressure tabs. In sections 1 and 2, very small effects of the VGs array are visible for both the experiments and CFD. A good agreement between experiments and simulations can be appreciated. More interesting is the characterisation of the VGs effects on the wall pressure field at sections 3 and 4. As anticipated by the CFD analysis, for section 3 intersecting the backdoor surface downstream the VGs array, a clear increase of the pressure can be observed from both experiments and CFD where the flowfield is further decelerated. Note that the pressure rise between the clean geometry and VGs is quite similar in the experiments and in the simulations. The low pressure peaks found on this section by CFD and related to the formation of longitudinal vortices (see Fig. 4) are not captured by measurements due to a local lack of pressure taps. A pressure field increase can be also highlighted more easily at section 4 by plotting separately CFD results(bottom left) and experiments (bottom right). As indicated with arrows oriented upwards and downwards, a pressure rise is achieved in average with VGs, as found by experiments. Additionally, on this section the local pressure-tap distribution allows to capture the pressure peaks associated with the longitudinal vortices

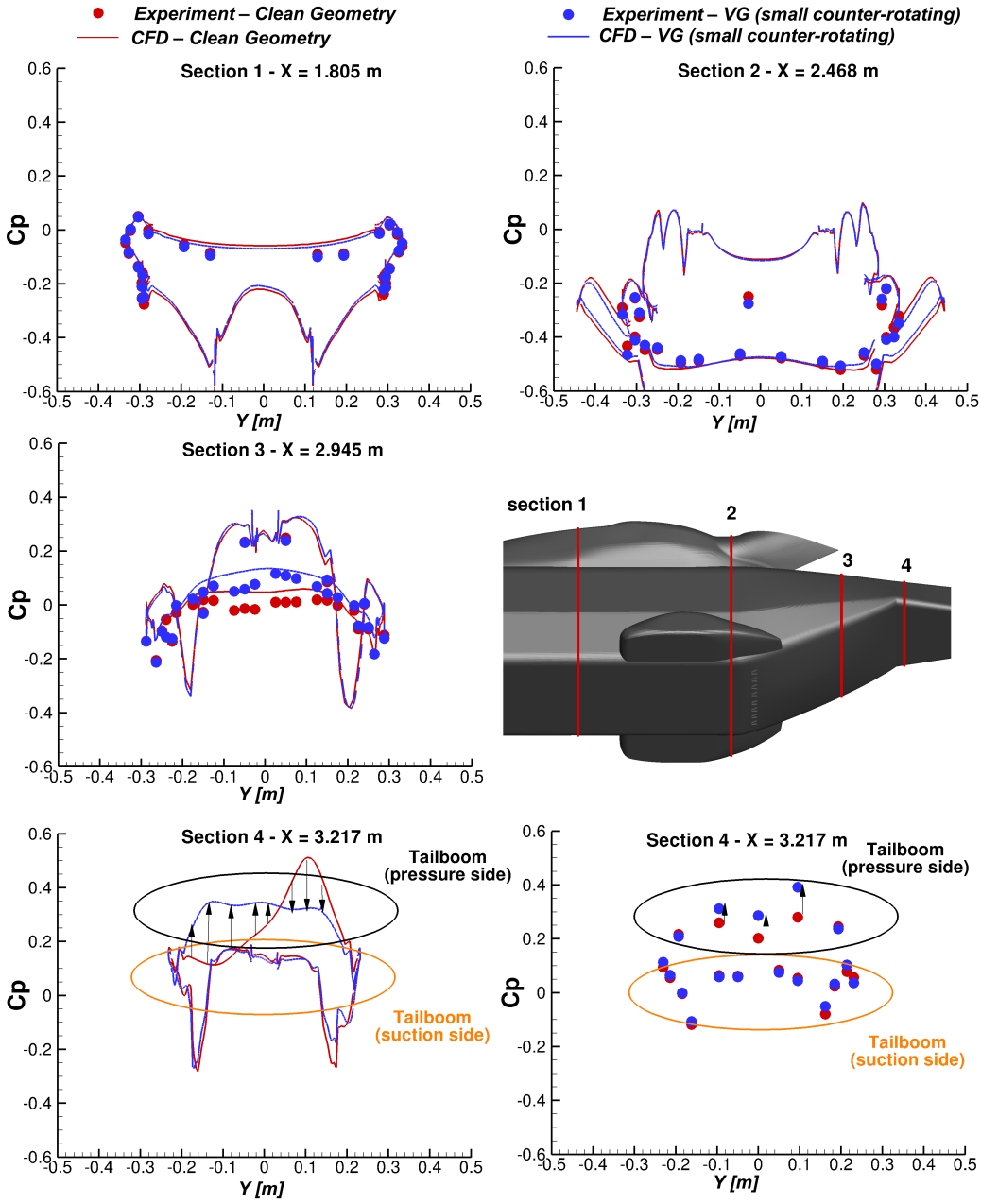

Figure 30: Experiments/CFD comparison at $\alpha = 2°$ for the Cp distribution at selected fuselage sections.

also in the measurements.

Due to a non-symmetrical topology of the separated flow computed by CFD, pressure distribution evaluated for the clean geometry on the tail boom pressure side downstream the junction with the backdoor results non-symmetrical. As for the PIV, a more symmetric distribution was measured in the experiments on this section. Similarly to what done for the PIV measurements a symmetrised solution was computed by averaging the non-symmetrical CFD pressure distribution with its mirrored distribution with respect to the X-Z plane at $Y = 0$ m. A good agreement of the symmetrised solution with the measured mean pressure distribution is apparent for this section (see Fig. 31). The pressure recovery due to the VGs (blue dotted line) is especially well reproduced in average by the CFD solution at the tailboom pressure side.

5. Conclusions

Drag reduction of a heavy-class helicopter fuselage model by vortex generators predicted at ONERA by preliminary CFD computations was confirmed within a comprehensive test campaign for aerodynamic loads, velocity field and static pressure carried out at the wind tunnel test facility GVPM of Politecnico di Milano. The best results were found for an array of 8 pairs of delta-scale counter-rotating VGs located in the lower backdoor area, slightly downstream of the upsweep line characterising blunt helicopter fuselages, and upstream the large separated flow occuring at the junction backdoor/tail boom for the clean geometry. A significant drag reduction of about 5% was measured for angles of attack close to 0°. For the angle of attack $\alpha = 2°$

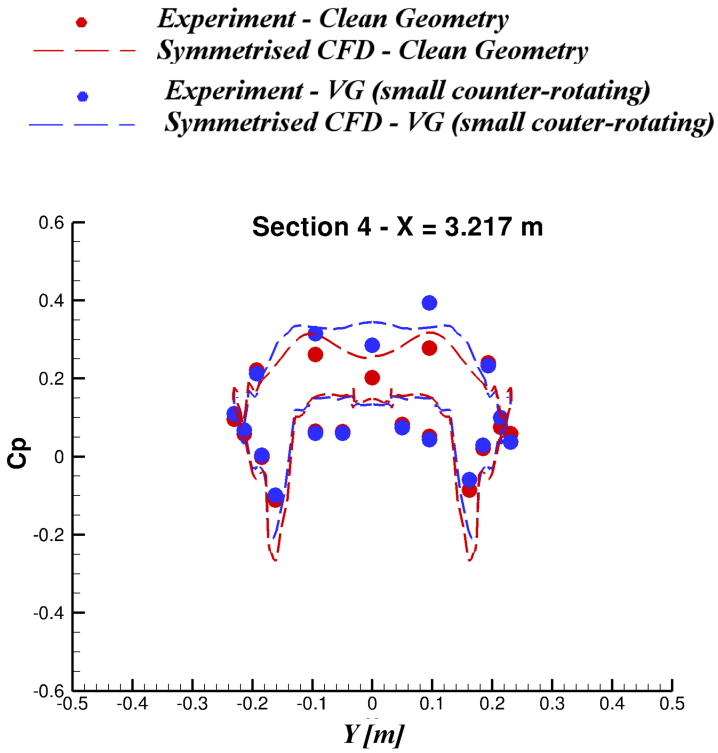

Figure 31: Comparison of the symmetrised CFD solution with the mean measured Cp distribution on section 4 at $\alpha = 2°$.

especially investigated in this paper, PIV measurements show that the VGs promote the reattachment of the flow around the back-ramp. In fact, the flow in the measurement volume of investigation does not show separations, while a limited flow recirculation is still predicted by RANS computations in the near-wall region. Furthermore, a fundamental effect of VGs anticipated by CFD consisting in static pressure recovery in the backdoor area is fully confirmed by experiments. It was especially shown that VGs trigger a smooth increase of the adverse pressure gradient along the backdoor while they re-energise the boundary layer, thus preventing flow separation. This result confirms the potential benefit of VGs in reducing the suction effect responsible for pressure drag at the fuselage after-body. The good agreement shown with experiments confirms the reliability of the CFD approach for such kind of studies.

6. Acknowledgements

The research leading to these results has received funding from the European Community's Seventh Framework Programme (FP7/2007-2013) for the Clean Sky Joint Technology Initiative under grant agreement n. 325997.

References

[1] Allan, B.G., Schaeffler, N.W., 2011. Numerical investigation of rotorcraft fuselage drag reduction using active flow control, AHS 67th Annual Forum, Virginia Beach, VA.

[2] Bender, E., Anderson, B., Yagle, P., 1999. Vortex generator model-

ing for navier-stokes codes, 3rd joined ASME/JSME Fluids Engineering Conference, San Francisco, CA.

[3] Benek, J.A., Steger, J.L., Dougherty, F.C., 1983. A flexible grid embedding technique with application to the euler equations, 6th Computational Fluid Dynamics Conference, Danvers, MA.

[4] Boniface, J.C., 2014. A computational framework for helicopter fuselage drag reduction using vortex generators, AHS 70th Annual Forum, Montréal, Canada.

[5] Boniface, J.C., Joubert, G., Le Pape, A., 2013. Passive flow control by vortex generator for internal and external aerodynamics configuration, 48th International Symposium of Applied Aerodynamics, Saint-Louis, France.

[6] Cambier, L., Heib, S., Plot, S., 2013. The onera elsa cfd software: Input from research and feedback from industry. Mechanics & Industry 14, 159–174.

[7] Chima, R.V., 2002. Computational Modeling of Vortex Generators for Turbomachinery. NASA TM 211551.

[8] Gregorio, F.D., Pengel, K., K., 2012. A comprehensive piv measurement campaign on a fully equipped helicopter model. Experiments in Fluids 53, 37–49.

[9] Gustavsson, T., 2006. Alternative Approaches to Rear End Drag Reduction. KTH Technical Report TRITA-AVE 2006:12. Department of

Aeronautical and Vehicle Engineering, Royal Institute of Technology, Stockolm.

[10] Gustavsson, T., Melin, T., 2006. Application of Vortex Generators to a Blunt Body. KTH Technical Report TRITA-AVE 2006:13. Department of Aeronautical and Vehicle Engineering, Royal Institute of Technology, Stockolm.

[11] Le Pape, A., Costes, M., Joubert, G., David, F., Deluc, J.M., 2012. Dynamic stall control using deployable leading-edge vortex generators. AIAA Journal 50, 2135–2145.

[12] Lienard, C., Allan, B., Pape, A.L., Schaeffler, N., 2015. Comparing numerical and experimental results for drag reduction by active flow control applied to a generic rotorcraft fuselage, AHS 71st Annual Forum, Virginia Beach, VA.

[13] Lin, J.C., 2002. Review of research on low-profile vortex generators to control boundary-layer separation. Progress in Aerospace Sciences 38, 389–420.

[14] Mai, H., Dietz, G., Geissler, W., Richter, K., Bosbach, J., Richard, H., Groot, K.D., 2008. Dynamic stall control by leading edge vortex generators. Journal of the American Helicopter Society 53, 26–36.

[15] Martin, P., Berry, J., Wong, T.C., Moulton, M., McVeigh, M., 2008. Passive control of compressible dynamic stall, 26th AIAA Applied Aerodynamics Conference, Honolulu, Hawaii, USA.

[16] Menter, R., 1994. Two-equations eddy-viscosity turbulence model for engineering applications. AIAA Journal 32, 1598–1605.

[17] Ortmanns, J., Pixberg, C., Gummer, V., 2011. Numerical investigation of vortex generators to reduce cross passage flow phenomena in compressor stator endwalls, European Turbomachinery Conference, Istanbul, Turkey.

[18] Paul, A., Kuppa, K., Yadav, M., Duta, U., 2011. Flow improvement in rectangular air intake by submerged vortex generators. Journal of Applied Fluid Mechanics 4, 77–86.

[19] Péron, S., Benoit, C., 2013. Automatic off-body overset adaptive cartesian mesh method based on an octree approach. Journal of Computational Physics 232, 153–173.

[20] Pesteil, A., Cellier, D., Domercq, O., Perrot, V., Boniface, J.C., 2012. Create: Advanced cfd for hpc performance improvement, ASME Turbo Expo, GT2012-68844.

[21] PIVTEC, 2010. Pivview 2C/3C. User Manual www.pivtec.com.

[22] Raffel, M., Gregorio, F.D., Groot, K.D., Schneider, O., Sheng, W., Gibertini, G., Seraudie, A., 2011. On the generation of a helicopter aerodynamic database. Aeronautical Journal 115, 103–112.

[23] Raffel, M., Willert, C., Kompenhans, J., 1998. Particle Image Velocimetry, a practical guide. Springer, Heidelberg.

[24] Xue, S., Johnson, B., Chao, D., Sareen, A., Westergaard, C., 2010. Advanced aerodynamics modeling of vortex generators for wind turbine applications, European Wind Energy Conference (EWEC), Warsaw, Poland.

[25] Zanotti, A., Ermacora, M., Campanardi, G., Gibertini, G., 2014. Stereo particle image velocimetry measurements of perpendicular blade-vortex interaction over an oscillating airfoil. Experiments in Fluids 55, 1811–1–13.

[26] Zheng, X., Liao, C., Liu, C., Sung, C., Huang, T., 1997. Multigrid computations of incompressible flows using two-equation turbulence models: Part i–numerical method. Journal of Fluids Engineering , 119:893–899.